XLVI CILAMCE
VITÓRIA - ES - BRAZIL - 2025
XLVI IBERO-LATIN AMERICAN CONGRESS ON COMPUTATIONAL METHODS IN ENGINEERING

Nonlinear instability analysis of long-span arcs – case-study

Warlley S. Santos [1], Eleir M. Bortoleto [2]

[1] *Dept. of Project, Vale S.A.*
Av. Dante Michelini, 5500 Ponta de Tubarão, 29090 900, ES/Vitória, Brazil
warlley.santos@vale.com
[2] *Vale Technological Institute, ITV-Mining*
Rua Prof. Paulo Magalhães Gomes. S/N, 35400-000, MG/Ouro Preto, Brazil
eleir.bortoleto@itv.org

Abstract. The study presents numerical findings concerning 3D long-span roofing models. These findings combine eight load cases that encompass both horizontal and vertical nodal component forces, as well as two boundary conditions applied to the arc bases: perfect hinges and fully fixed supports. Nonlinear analysis was conducted to evaluate postbuckling behavior and better estimate the safety factor. The analysis includes initial imperfections and nonlinear materials resulting in the following outcomes: equilibrium paths (relationship between reactions and arc center node displacements), deformed shape (type of collapse), and peak loads.

Keywords: Long-span roofing; Arc buckling; Numerical analysis; Nonlinear instability.

1 Introduction

Due to population growth, housing approaches industrial zones, intensifying the demand to decrease air pollution emissions. Consequently, an increasing number of storage yards are being covered [1]. Under this fact, the utilization of long-span steel arc structures is prevalent, as they facilitate many architectural designs enabling their construction above material handling yards while operations occur simultaneously.

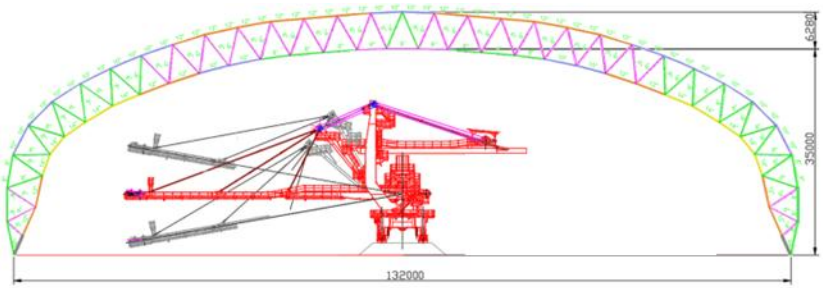
This type of roofing inevitably addresses instability problems. Arc instability can be classified by snap-through and in-plane or out-of-plane buckling. Snap-through buckling is usually observed in cases of shallow arcs, with orthogonal constraints to the plane of the same. In-plane buckling is the prevailing behavior in nonshallow arcs, also with orthogonal constraints to the arc plane. Out-of-plane buckling is observed generally in arcs that exhibit a significant portion unlocked laterally. This instability type is characterized by a combination of buckling in flexural and lateral-torsional modes [2]. Because of this, a complete non-linear buckling analysis is crucial for correctly predicting structural behavior [3].

As reported by Carpinteri et al. [3], is observed that studies typically focus solely on vertical loads. However, large-span roof structures are extremely sensitive to wind [4] since it is characterized as light and flexible, which suggests that horizontal component loads should be analyzed to take into account wind effects. Thus, the present study considers the structural response generated by load cases (LCs) with wind actions, analyzing the behavior of 3D arc steel structures with large roofing under the action of these different LCs and two boundary conditions for arc bases, namely, fully fixed supports and perfect hinges.

2 Arc geometry and load

The primary objective of this study was to carefully choose the arc for numerical analysis. The selected arc exhibits a span of 132 m and a free height of 35 m at its midpoint, enabling it to accommodate the operation of a 48 m boom stacker. Figure 1 shows the long-span roofing cross-section and the tubular elements (highlighted by colors) used to compose the arcs.

The distance between arcs is 10 m, while the distance between the purlins (cold-formed steel-lipped channel 300 x 85 x 25 x 4.8 mm) is 2.85 m. Three tie rod lines (∅ 12.7 mm) and a trapezoid metal tile form the structure. Roof bracing was installed every 60 m with a round bar (∅ 12.7 mm), and the arc bottom chord was laterally locked by using pipes (the outside diameter=73 mm; wall thickness=5.16 mm).



Section name	Outside diameter	Wall thickness
6″	168.3	7.11
8″	219.1	8.18
10″	273.0	9.27
12″	323.9	10.31
14″	355.6	11.30
22″	559.0	28.58

Figure 1. Cross section of the long-span roofing with tubular elements (mm)

All internal arc links between chords and webs are represented by rigid connections. Two extreme basis conditions are considered in this paper: (i) perfect hinges and (ii) fully fixed supports.

The live load follows ABNT NBR 6120 [5], and the wind load follows ABNT NBR 6123 [6], which are Brazilian codes equivalent to American code ASCE/SEI7–10 [7]. Eight LCs are considered combinations of dead, live, and wind loads to be analyzed numerically in this paper following ABNT NBR 8800 [8] code (the correlated American standard is ANSI/AISC 360-16 [9]). Figure 2 represents these LCs qualitatively. All arc components were previously verified according to Eurocode 3 [10] considering the eight LCs under both basis conditions.

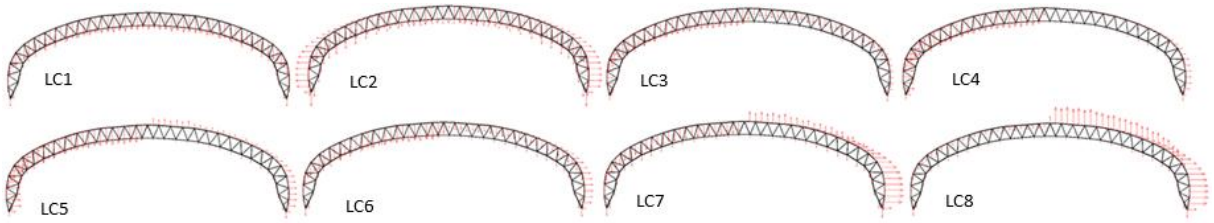


Figure 2. Nodal forces for each load case

3 Numerical investigation

In this section, numerical finite element methodologies are presented for buckling, postbuckling, and ultimate strength analysis. Additionally, the mechanical behavior of a long-span arc is also examined under different load cases subject to buckling under two different boundary conditions: the first boundary condition considers perfect hinges, while the second one evaluates the condition of fully fixed supports.

Nonlinear finite element analysis carried out via ANSYS code [11] was used to determine the arc postbuckling equilibrium paths. Models were also able to determine the arc ultimate strength by considering geometric imperfections and non-linear material. The Finite Element mesh for the arc members considered 4336 ANSYS BEAM188 elements (beam elements with 2-nodes, shear deformable, with 6 degrees of freedom for each node: translations and rotations in the nodal x, y, and z directions) suitable for analyzing stability problems. Accurate results were obtained by discretizing the arc member into a 730 mm maximum element size. The other 421 bars (disregarding the arc members) were discretized using one element per bar (ANSYS element type LINK180, with 2-nodes, uniaxial tension-compression, 3 degrees of freedom at each node: translations in the nodal x, y, and z directions). Additionally, the SHELL181 element (full integration 4-node shear deformable thin-shell element, 6 degrees of freedom per node) represented the roof tile (0.1 mm thickness) – 768 shell elements. The 3D models were considered with four arcs to obtain reliable and converged results with less computational processing time. The total element number in each model is 5525. Figure 3 shows this geometry.

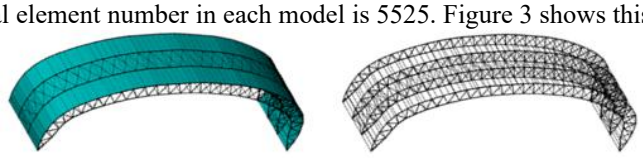


Figure 3. 3D model geometry with and without shell elements respectively

3.1 Eigen Buckling Analysis

For each LC, two distinct boundary conditions, namely double-hinged and fully restrained arcs, were established in the models. The material properties employed in the analysis included an Elastic modulus (E) of *20000 kN/cm²* and Poisson's ratio (v) of *0.3*. A linear elastic static analysis was performed to determine the stiffness matrix. Subsequently, the eigenvalues and autovector analysis were performed to ascertain the deformed configurations (in a qualitative perspective) of elastic buckling and the relationship between the applied load and the elastic buckling load. This procedure enabled us to obtain the critical buckling numerical multiplier loads, λ; these values are shown in Table 1.

Table 1. Multiplier factor λ for each LC considering double-hinged and fully restrained arc bases

Load case	Perfect hinges	Fully fixed
LC1	4.34	4.57
LC2	6.51	6.88
LC3	4.83	5.43
LC4	5.12	6.05
LC5	6.97	7.70
LC6	4.30	4.84
LC7	5.89	6.54
LC8	7.71	8.50
MAX.	7.71	8.50
MIN.	4.30	4.57

The minimum multiplier value reached is 4.30 for perfect hinged LC6. This means that this particular LC is the most sensitive to buckling. In this case, horizontal forces act in a single direction while vertical actions in the half arc are in the gravity direction, and the opposite occurs in the other half arc. This type of asymmetric loading provides minimum values for λ. On the other hand, the maximum λ value estimates are 7.71 and 8.50 for LC 8 for perfect hinged and fully fixed arcs, respectively. This means that LC 8 is less sensitive to buckling.

Another point is that the λ values for the fully fixed bases were consistently higher than those for the perfectly hinged arc bases. Therefore, fully fixed bases are less sensitive to buckling than perfectly hinged ones.

Figure 4 shows the qualitatively deformed forms of elastic buckling analyses for pinned and fixed arc bases for each LC. There is a difference in the response trend of LCs 1, 2, 3, 4, and 6 when compared to LCs 5, 7, and 8. In all 3D model cases, the maximum deformation elastic buckling occurs in the bottom chords. In all cases, out-of-plane elastic buckling is observed.

The pairs of letters MN and MX in Figure 4 represent the minimum and maximum displacement in the qualitatively deformed forms of elastic buckling, respectively. Additionally, no difference was observed between the qualitatively deformed forms considering the two different boundary conditions for the same LC.

This similarity observed in the deformed configurations for LCs 1, 2, 3, 4, and 6 can be attributed to the similarity between these LCs, as shown in Figure 2. A similar observation can be made regarding the deformed configurations of LCs 5, 7, and 8 for both models and the two adopted boundary conditions.

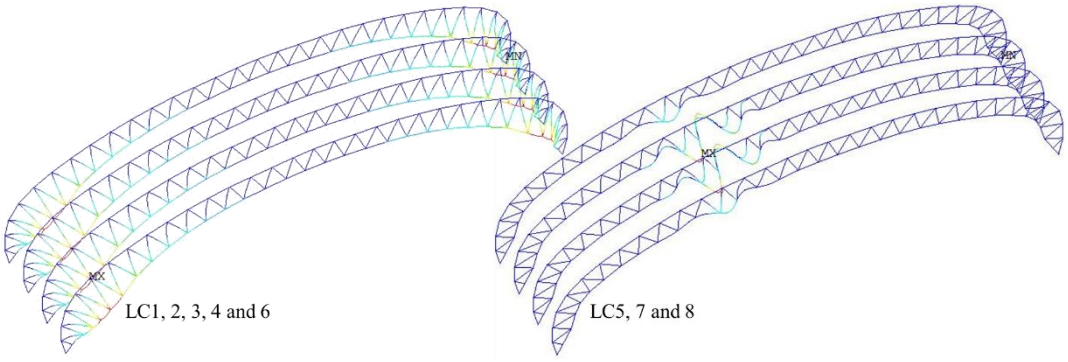


Figure 4. Qualitatively deformed forms of elastic buckling

3.2 Postbuckling Analysis

All postbuckling analyses were performed by adopting an incremental and iterative procedure that combines *Newton–Raphson's* method with an *arc-length* control technique. Using this procedure and the ANSYS automatic load stepping technique [11], forces are always increased in small increments.

The critical-mode initial equivalent geometrical imperfections in the arcs were made using the following procedure. First, the critical buckling mode shape was determined via a finite element eigen-buckling analysis. Then, this mode shape was scaled to exhibit maximum displacements equal to *L/300*, where *L* represents the component length that presented the maximum displacement. This amplitude is according to Eurocode 3 [10].

The postbuckling analysis was divided into two: elastic and elastic-plastic analyses with ultimate strength. The objective of the elastic postbuckling analysis is to determine the postbuckling behavior of an elastic material; the main result is the elastic equilibrium path. The analyses of the elastic equilibrium trajectories for arcs under pinned bases and fixed-base boundary conditions make it possible to resolve the buckling mode (global arc or arc's components). The elastic-plastic models exhibited a response that was elastic-perfectly plastic for the material behavior (which followed the *Prandtl-Reuss*'s model, which considers a *von Mises* yield criterion and an associated flow rule) by adopting steel with yield stress $fy=25\ kN/cm^2$ and a *von Mises* plasticizing criterion [12]. Further to the equilibrium path, the main result of the elastic-plastic postbuckling analysis is the ultimate strength, which is defined as the highest vector sum module reaction force reached in the elastic-plastic trajectory of the equilibrium.

From the previously presented methodology, the next paragraphs describe the numerical study results. These sections include an elastic postbuckling analysis to determine the lower equilibrium path, an elastic-plastic postbuckling analysis, with a collapse mechanism, and a comparison between models with pinned and fixed bases.

To show the elastic postbuckling equilibrium path results and to evaluate the qualitative and quantitative aspects of how the support conditions influence the arc elastic postbuckling behavior, Figure 5 shows the postbuckling equilibrium paths of all LCs exhibiting the two boundary conditions addressed in this work. These equilibrium paths plot the vector sum of base reactions, $\sum VR$, against the total displacement δ occurring along the midpoint of the bottom chord arc. The examination of these eight sets of two elastic postbuckling equilibrium trajectories suggests the following remark: the lower equilibrium path is always along the pinned arc bases; this is to be expected due to the lower stiffness in the base connection.

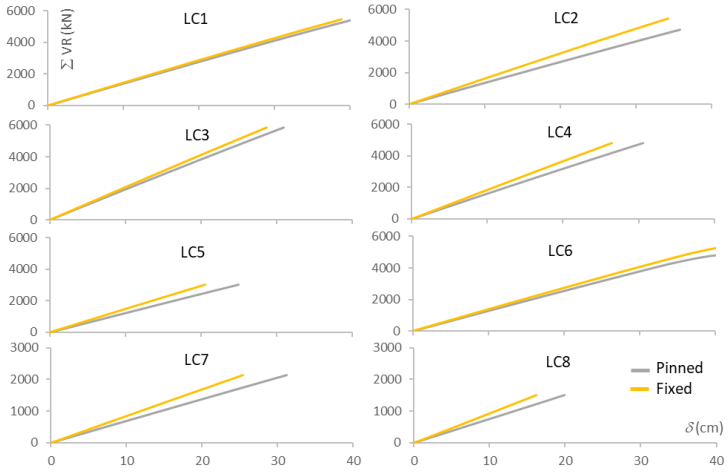


Figure 5. Elastic equilibrium path $\sum VR$ vs. δ to arcs under pinned and fixed base conditions considering all LCs

The qualitative and quantitative influence of the base supports and load cases on the arc elastic–plastic postbuckling and ultimate strength behavior were examined. Arcs with different LCs presented in item 2 are discussed, considering the material mechanical properties and the initial imperfection as critical buckling, which is presented in this section (item 3.2).

Table 2 shows for each boundary condition (i) the vector sum of base reactions ($\sum VR_total$) and (ii) the relationship between the ultimate load (*Pu*, obtained from non-linear analysis) and the $\sum VR_total$ with the corresponding minimum and maximum values.

Table 2. Vector sum of the base reactions and ultimate load ratios for perfect hinges and fully fixed bases

Load case	$\sum VR_total$ (kN)	$Pu/\sum VR_total$ Perfect hinges	$Pu/\sum VR_total$ Fully fixed
LC1	1822.31	2.00	2.07
LC2	1182.71	3.06	3.12
LC3	1955.14	2.35	2.56
LC4	1594.58	2.62	2.98
LC5	1000.24	2.51	2.78
LC6	1459.35	2.13	2.30
LC7	711.14	2.10	2.34
LC8	500.69	2.67	2.67
MIN.	500.69	2.00	2.07
MAX.	1955.14	3.06	3.12

As stated in section 2, all cross-section arc components were verified considering all eight LCs and both basis conditions according to Eurocode 3 [10] on static analysis. An analysis of Table 2 shows that all $Pu/\sum VR_total$ values are higher than 2.0, which provides a postbuckling reserve estimation when conducting nonlinear geometric and elastic-plastic postbuckling analyses.

Figure 6 shows, for all LCs, the in-plane deformed shapes with undeformed arcs. These deformed shapes have been amplified by a factor of 18.5 and are in accordance with the loadings represented in Figure 2.

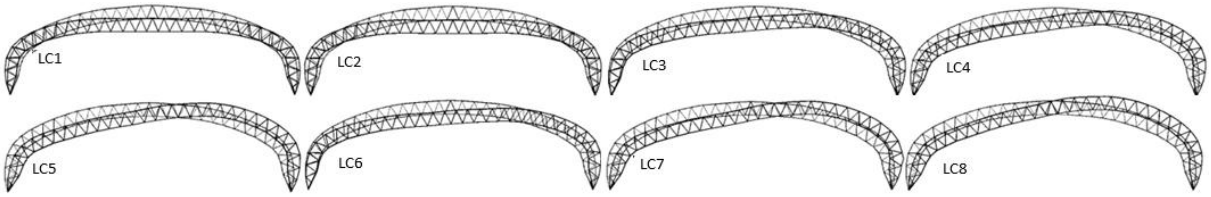


Figure 6. Arc deformed shapes with undeformed models under pinned and fixed base conditions for all LCs

Since the LCs analyzed shared the same structural behavior, just a representative sample of these different numerical results are singly reported and debated in the following paragraphs.

Figure 7 displays the results, for each base support type, and for selected LCs, considering the geometric and material nonlinearities, of the equilibrium trajectories. The equilibrium trajectories were determined to obtain the ultimate loads *Pu* (identified by circles). These selected equilibrium paths represent the pinned and fixed base arcs for LCs 2, 4, 5, and 8. Here, the sum of the vectorial reaction gives the ordinate axis applied for each step, normalized by the vectorial reaction total sum, since the abscissa is the given total displacement δ (cm).

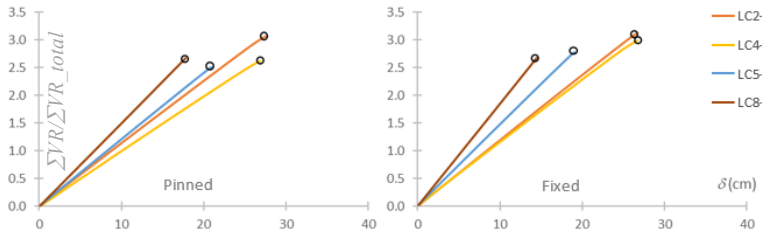


Figure 7. Elastic-plastic equilibrium paths ($\sum VR/\sum VR_total$ vs. δ) concerning pinned and fixed base arcs

Figures 8 and 9 depict the deformed arc configurations that occur near to the peak points of each equilibrium trajectory displayed in Figure 7 for pinned and fixed base conditions respectively. Additionally, this figure shows *von Mises* equivalent stress distribution (kN/cm²). Notably, the deformations were amplified by a factor of 18.5.

Figures 10 and 11 show the elastic-plastic equilibrium trajectories, considering pinned and fixed bases and Load Case 5, presenting the evolution of its deformed configuration. The *von Mises* equivalent stress distributions are also presented (marked as *I* at the beginning of yield and *II* at the ultimate load) – kN/cm². The amplitudes of

the deformed configurations have been scaled by a factor of 18.5. By analyzing the results regarding the elastic-plastic postbuckling and ultimate strength presented in Figures 7 to 11, some conclusions can be drawn:

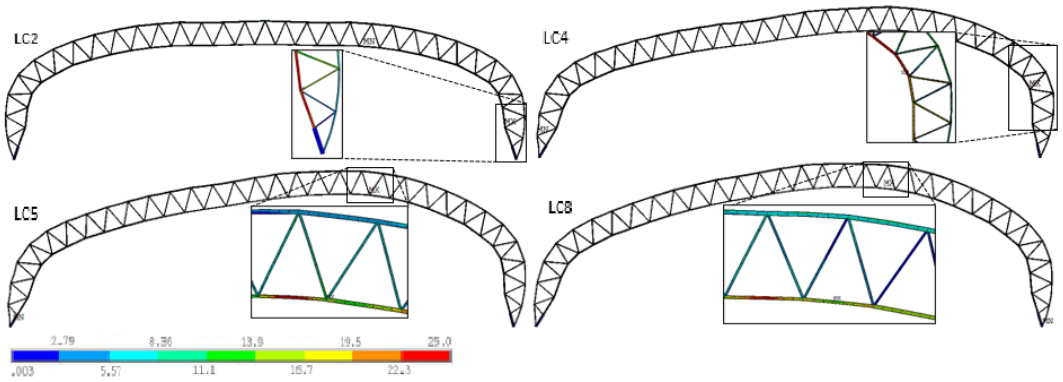


Figure 8. Global failure modes and *von Mises* stress distribution (kN/cm²) for LC 2, 4, 5, and 8 – pinned arcs

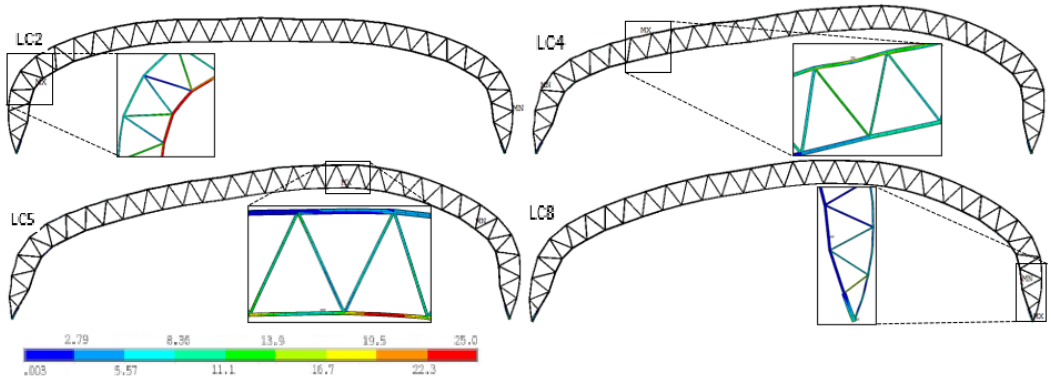


Figure 9. Global failure modes and *von Mises* stress distribution (kN/cm²) for LC 2, 4, 5, and 8 – fixed arcs

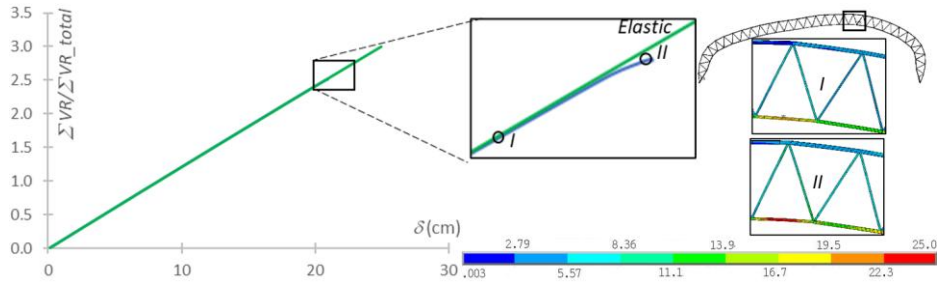


Figure 10. Equilibrium path for elastic and elastic-plastic behavior with collapse mechanism - pinned arc LC5

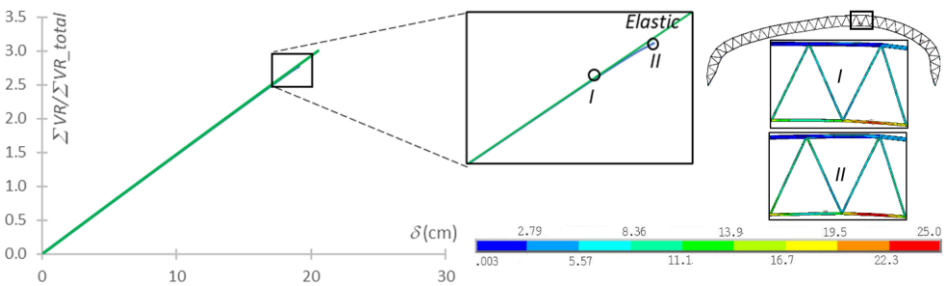


Figure 11. Equilibrium path for elastic and elastic-plastic behavior with the collapse mechanism - fixed arc LC5

i. There is a considerable linear portion in the equilibrium paths $\sum VR/\sum VR_total$ vs. δ shown in Figure 7. Here, the slopes are different from each other, thus demonstrating different structural responses for each LC.

ii. Figures 8 and 9 depict the deformed arc settings that occur close to the ultimate point for each equilibrium path described in Figure 7. These data demonstrate an accurate representation of the failure mode namely global out-of-plane buckling on the truss elements. For each LC and boundary condition, the nature of the failure is not always the same mode shown by the eigen buckling analysis.

iii. For LC5, Figures 10 and 11 show that yielding begins at the lateral midpoint chord elements, as shown in stage *I*. While loading increases, according to the arcs present, the deformed yield progress in the arc member, with continuing charging, facilitates the formation of one "global plastic hinge" in this arc member, as shown in stage *II*. Stages *I* and *II* can be found on the right side of Figures 10 and 11.

4 Conclusions

In this paper, the numerical results of simulations concerning long-span roofing structures are reported. Eight LCs were considered by combining horizontal and vertical forces and two boundary conditions for arc bases (perfect hinges and fully fixed supports), taking into account linear and non-linear analyses.

For each load case, a linear buckling analysis was carried out, and the critical factor λ was determined under two different restraining conditions. Compared with the fully restrained condition, the simulations demonstrated that the double-hinged arc boundary condition always presents lower critical loads.

For the elastic postbuckling analysis presented in this work, the lower equilibrium path was always in the pinned arc bases. This behavior was to be expected due to the lower stiffness in the base connections.

Finally, nonlinear analysis was conducted for model arcs under the two previously reported restraining conditions. The results demonstrate that considering elastic–plastic postbuckling analysis, the collapse mechanisms observed in arc members are always global buckling out-of-plane. Additionally, the critical loads calculated from the linear analysis were compared, which showed that the maximum load obtained from the non-linear model is always lower. Therefore, by performing only linear buckling analysis the structural safety factor will be overestimated. Nonlinear analysis is the most suitable method to evaluate the safety factor of this kind of structure.

Acknowledgments. The authors acknowledge the financial support of Vale S.A.

Authorship statement. The authors hereby confirm that they are the sole liable persons responsible for the authorship of this work and that all material that has been herein included as part of the present paper is either the property (and authorship) of the authors or has the permission of the owners to be included here.

References

[1] N. Su, S. Peng, N. Hong e T. Hu, “Wind tunnel investigation on the wind load of large-span coal sheds with porous gables: Influence of gable ventilation,” Journal of Wind Engineering & Industrial Aerodynamics, 2020.
[2] I. D. Thanasoulas e C. J. Gantes, “Stability criteria for roller-bent circular-hollow-section steel arches,” Journal of Constructional Steel Research, pp. 1-11, 2020.
[3] A. Carpinteri, F. Bazzucchi and A. Manuello, "Nonlinear instability analysis of long-span roofing structures: The case-study of Porta Susa reilway-station," Engineering Structures, pp. 48-58, 2015.
[4] N. Su, S. Peng e N. Hong, “Analyzing the background and resonant effects of wind-induced responses on large-span roofs,” Journal of Wind Engineering & Industrial Aerodynamics, pp. 114-126, 2018.
[5] ABNT NBR 6120, Ações para cálculo de estrutura de edificações, Rio de Janeiro: ABNT, 2019.
[6] ABNT NBR 6123, Forças devido ao vento em edificações, Rio de Janeiro: ABNT, 2013.
[7] ASCE/SEI 7-10, Minumum Design Loads for Buildings and Other Structures, Virginia, USA: American Society of Civil Engineers ASCE Standard, 2010.
[8] ABNT NBR 8800, Projeto de estruturas de aço e de estruturas mistas de aço e concreto de edifícios, Rio de Janeiro: ABNT, 2008.
[9] ANSI/AISC 360-16, Specification for Structural Steel Buildings, Chicago, Illinois: AISC Committee on Specifications, 2016.
[10] Eurocode 3, Design of steel structures - Part 1-1: General rules, Brussels: EUROPEAN STANDARD, 1993.
[11] Swanson Analysis System Inc., (SAS), Ansys Reference Manual (Vrs. 15), 2015.
[12] S. P. Timochenko and J. M. Gere, Theory of Elastic Stability, Tokyo: Tosho Printing Co.,LTD., 1961.